Reconfiguring a Modular Robot into a Humanoid Formation: A Multi-Body Dynamic Perspective on Motion Scheduling for Modules and their Assemblies

Paul M. Moubarak, *Student Member, IEEE,* Eric J. Alvarez, Pinhas Ben-Tzvi, *Senior Member, IEEE*

***Abstract*—In this paper, we study the scheduling architecture that enables an assembly of mobile modules to re-configure into a humanoid formation with a manipulator arm. The investigated problem arises from the articulated nature of the formation which involves multiple degrees of freedom, thus requiring a control approach that synchronizes the actuators' motion during shape metamorphosis. Using the principles of motion kinematics and caterpillar tracks modeling, we present a coherent solution which we further validate on a sample three-module formation of STORM (Self-configurable and Transformable Omni-directional Robotic Modules). Simulation results on MSC ADAMS CAR validate the feasibility of the synchronization architecture, and offer further insight into the dynamic dependencies of coupled motions.**

I. Introduction

IN MODULAR ROBOTICS [1], the high number of actuators involved in the motion generation of a given formation is a byproduct of the aggregate individual actuators that each swarm member contributes to the assembly. In the event of a highly articulated formation, the ensuing number of degrees of freedom prohibits the manual control of the assembly, as the ensemble of simultaneous commands involved in the generation of a desired motion grows proportionally with the total number of actuators [2].

Central to the control of multi-agent formations is an architecture that synchronizes the motion of individual members. In fact, motion synchronization is a ubiquitous control scheme that can be exemplified in many observations, such as in nature's collective animal behavior and in neuro-mechanical control of movement [3]. For example, schooling in marine biology is a coordinated behavior that synchronizes the speed of small fish to create a large formation with the intention of avoiding predation through confusion and size intimidation. Alternatively, in vertebrate physiology [4], the generation of motor activity is the derivative of a synchronized firing process of the neural system resulting in a deterministic behavior or movement, such as walking [5], breathing, *etc*.

This neuro-mechanical synchronous interface is controlled by a central pattern generator (CPG) [6], [7], which lies at the core of biomimetic research [8] on motion generation in articulated formations of rigid-structure [9] and modular robotics [10], [11]. However, CPG-based motion control is primarily applicable to the generation of oscillatory movements, such as swimming undulations [12], since the implementation of CPG requires the motion to be harmonic, with each actuator repeatedly returning to its original starting point. Therefore, for non-rhythmic motion, a non-CPG control scheme dictates a more fundamental kinematic approach for movement scheduling that further takes into consideration the dynamics of the formation.

In this paper, we are interested in such non-rhythmic behavior of modular robotic chains. In particular, we study the scheduling architecture that enables a three module configuration of STORM [13] to reshape into a humanoid formation. Given the antagonistic nature of some joints and the number of degrees of freedom involved in this assembly, we propose a scheduling architecture for joint motion and pulley velocities that consists of a sum of sequential actuations, weighted by corresponding step functions with parabolic rise time. Simulation results validate this approach, and offer further insight into the dynamic dependencies of simultaneous actuations that contribute to the overall process of shape metamorphosis.

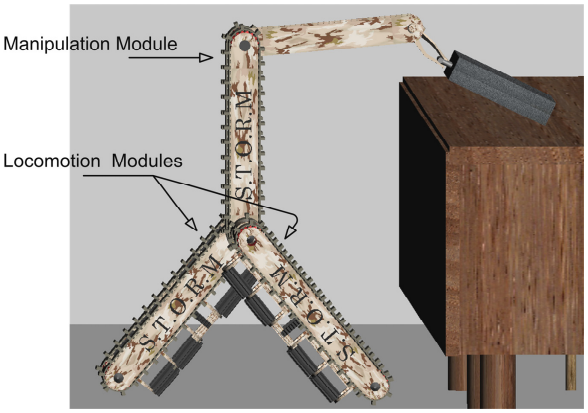

Fig. 1. A mock-up of STORM [13] in a humanoid formation during object manipulation

Manuscript received February 25, 2013. This work is supported by the Robotics and Mechatronics lab at the George Washington University, Washington, DC 20052, USA.

P. M. Moubarak is a Doctoral student in the Department of Mechanical and Aerospace Engineering at the George Washington University, Washington DC (Phone #: 202-321-7383; e-mail: paul4@gwu.edu)

E.J. Alvarez is an undergraduate student in the Department of Mechanical and Aerospace Engineering at the George Washington University, Washington DC (e-mail: paul4@gwu.edu)

P. Ben-Tzvi is an Assistant Professor of Engineering and the Director of the Robotics and Mechatronics Lab at the George Washington University, Washington DC (Phone #: 202-994-6149; e-mail: bentzvi@gwu.edu)

II. SYSTEM OVERVIEW AND CAE MODEL

A. Overview of STORM

The modular robot we study in this paper is STORM, which possesses an articulated structure inspired by the Hybrid Mechanism Mobile Robot [14] – [16]. STORM consists of two categories of independent mobile modules: a locomotion and a manipulation module, both shown in Figs. 1 and 2. The locomotion module comprises a wheeled unit in the middle which can translate vertically along a prismatic joint. This enables the module to selectively deliver hybrid multi-directional mobility via either the tracks (longitudinal), or the wheels (lateral), by toggling the mobility mode along the prismatic joint. Alternatively, the manipulation module can provide longitudinal tracked mobility with differential steering in the undocked configuration, and further carries a central one-link arm with an end-effector.

In a scaled formation, these two modules are coupled together via a docking interface [17], which creates a revolute joint between them, and enables one module to rotate relative to its neighbor in a chain architecture. Details about this docking process, the three operation modes of this interface and its rigidity can be found in [17], [18].

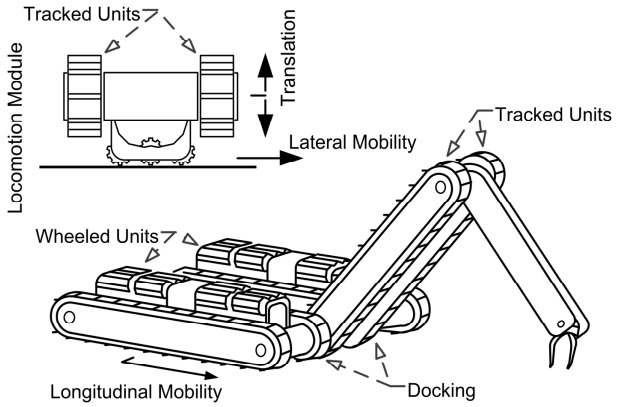

Fig. 2. Schematic of the locomotion and manipulation modules showing relevant mobility details

In particular, in this paper, we are interested in the motion synchronization of a three-module formation of STORM, referred to as STORM-3 (Fig. 1), and consisting of one manipulation module cascaded between two locomotion modules. A kinematic diagram of the *actuated* degrees of freedom of this formation is shown in Fig. 3, which involves a total of thirteen joints described as follows:

- Four revolute joints for the active pulleys of the locomotion modules (R_1 – R_4), where each pulley drives one of the two timing belts of every tracked unit.
- Four revolute joints to drive the wheels of the locomotion modules' wheeled units (R_5 – R_8).
- Two revolute joints at the docking interface (R_9 and R_{10}) between the locomotion modules and the arm, actuated by two separate motors.
- One revolute joint for the arm (R_{11}).
- One revolute joint for the pitch inclination of the end-effector (R_{12}).
- One revolute joint to open and close the fingers (R_{13}).
- Two prismatic joints (P_1, P_2) to toggle between the two mobility modes of the locomotion modules.

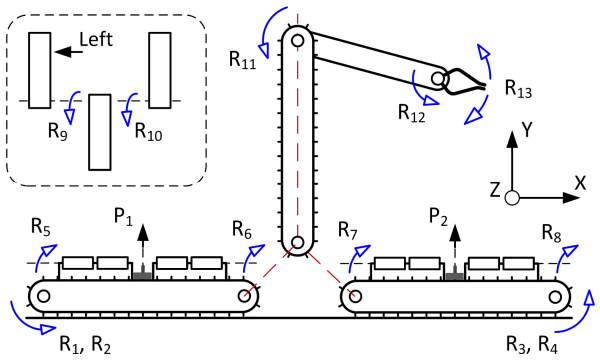

Fig. 3. Kinematic diagram of STORM-3 showing all revolute and prismatic joints

We note that in this paper, we are primarily interested in the motion scheduling of the joints that directly contribute to the reconfiguration of STORM-3 into a legged formation. This excludes the two joints of the end-effector, as well as the arm (R_{11}) and the wheel joints (R_5 – R_8).

B. 3-D CAE Model on MSC ADAMS CAR

To investigate the proposed synchronization architecture of STORM-3, we first modeled the locomotion and manipulation modules on MSC ADAMS CAR, which is a multi-body dynamics software platform providing track wrapping, tension optimization and simulation capabilities. The tracks' elasticity was capture by modeling them as a series of discrete segments coupled together through revolute joints. The rubber property of these segments further enables the tracks' wrapping around the active and passive pulleys, as well as the passive roller suspensions located in the middle of the tracked units. An example of such wrapping is depicted in Fig. 4 for the CAE model of the locomotion module, which also reflects the elasticity of the tracks when crossing a bump in the terrain (see simulation video in [19]).

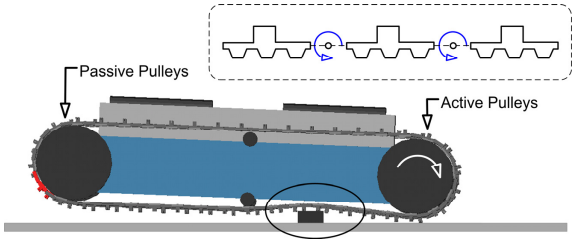

Fig. 4. CAE model of the locomotion module reflecting tracks' elasticity

Contacts between the track segments and the terrain are automatically generated by ADAMS CAR. In addition, contacts between the wheels of the wheeled units and the terrain are manually created, along with all the different revolute and prismatic joints that couple the different bodies

of STORM-3. The ensuing CAE model resulting from the integration of all subsystems is shown in Fig. 5, and will be subsequently adopted to analyze the proposed synchronization architecture. We note that pertinent mass and dynamic properties of the different subsystems involved in this assembly are summarized in Table 1.

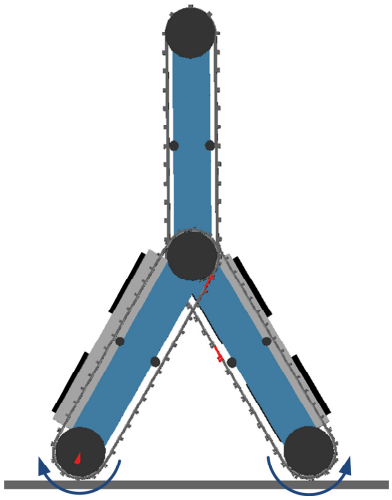

Fig. 5. A complete MSC ADAMS CAR model of STORM-3 with six track assemblies wrapped around corresponding pulleys and suspensions

Table 1. Table 2. Mass and polar moment of inertia of the different subsystems of STORM-3 in its ADAMS CAR model

	Mass (g)	Polar Moment of inertia about Z-axis, (g×mm^2) (×10^5)
Locomotion Module		
Active Pulley	276.0	1.956
Passive Pulley	170.0	1.189
Passive Suspension	24.3	0.0485
Track Segment	2.25	0.0225
Tracked Unit Chassis	4288	934.2
Wheeled Unit Chassis	2300	254.4
Wheeled Unit Wheel	11.0	1.625
Manipulation Module		
Active Pulley	211.3	1.659
Central Arm	2144.3	223.2
Passive Pulley	147.2	1.134
Track Segment	2.25	0.0225
Chassis	5580	969.6

III. DYNAMIC MODEL AND SCHEDULING ARCHITECTURE

To study the dynamics and motion synchronization of the humanoid formation of STORM-3, we take advantage of structural symmetry, and formulate the equations of motion for the left locomotion module only. Similar formulations can be extrapolated for the right module by symmetry.

A. Equations of Motion

A nomenclature is first defined in reference to Fig. 6 which depicts the free body diagram of the left locomotion module and its interaction with the arm. Thereafter, the superscript *L* will be used to designate the left module.

XYZ	Global Cartesian frame attached to the ground
L	Center-to-center length of the modules, equal to 400 mm in STORM-3
J, P	Points on the axes of joint R_9 and pulleys R_1 and R_2, respectively
${}^{L}d_C$	Distance between point J and the center of mass of the locomotion module
${}^{L}\psi, {}^{L}\theta$	Angular rotation of pulley joints R_1, R_2, and docking joint R_9 as a function of time, respectively
${}^{L}x$	Forward displacement of the left locomotion module
m_L, m_P	Mass of the locomotion module and active pulleys, respectively
m_M	Mass of the manipulation module
${}^{L}R$	Ground reaction acting on the left locomotion module
${}^{L}T$	Traction force generated by the active pulleys of the left locomotion module
${}^{L}f_{roll}$	Rolling friction force opposing the forward motion of the left locomotion module
${}^{L}\tau_P$	Drive torque generated by the active pulleys of the left locomotion module
τ_0	Pre-tension torque generated by the elasticity of the tracks around the drive pulleys
${}^{L}\tau_J$	Torque generated by the motor driving joint R_9
J_P, J_{LOK}	Polar moment of inertia of the active pulleys and the locomotion module about their respective center of mass

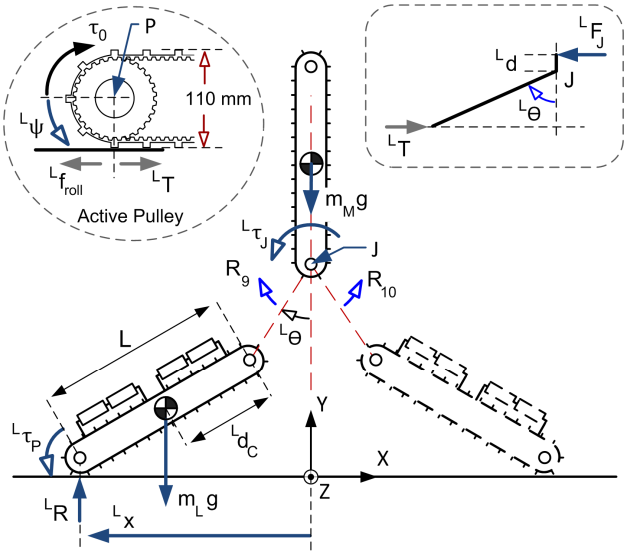

Fig. 6. Free body diagram of the left (L) locomotion module and the central manipulation module in the legged formation of STORM-3

For the humanoid formation, the reconfiguration process is split into three sequential stages as depicted in Fig. 7. The first stage involves the rotation of one locomotion module relative to both the arm and the other stationary module, while concurrently translating the corresponding wheeled unit to prevent interference with the ground (Fig. 7(b)). The second stage consists of rotating the central arm to a vertical posture relative to the two stationary locomotion modules (Fig. 7(c)-(d)), while the third stage involves the execution of a scissor-like motion that results in the desired humanoid formation, with the two locomotion modules providing leg support on the sides. It is this last stage that requires motion synchronization as the maneuver involves the simultaneous actuation of joints R_1 – R_4 and R_9, R_{10}.

With this nomenclature, a Lagrangian derivation of the kinetic and potential energies generated at Stage 3 yields an equation of motion for the active pulleys (Fig. 6) as

$$ {}^{L}\tau_P - {}^{L}f_{roll} r - {}^{L}F_J\left({}^{L}d + L\cos{}^{L}\theta(t)\right) - \tau_0 = J_P\ddot{\psi} \qquad (1) $$

where r defines the distance separating point P from the external track protrusions (55mm for the locomotion module). ${}^{L}F_J$ denotes the force generated by the applied torque ${}^{L}\tau_J$, where ${}^{L}F_J = {}^{L}\tau_J / {}^{L}d$, with ${}^{L}d$ depicting the corresponding lever arm (Fig. 6). This force opposes the forward motion of the locomotion module, and behaves as a wall reactive force in the event of an asynchronous motion (see the traditional latter example for instance [20]).

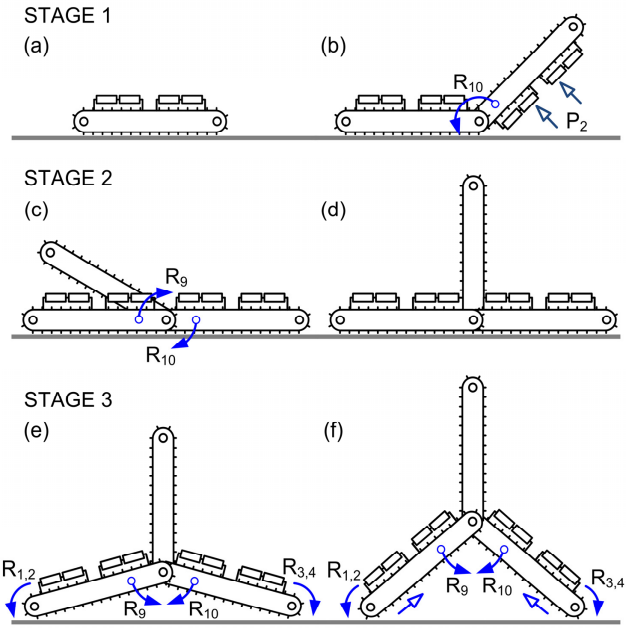

Fig. 7. A sequence of actuations showing the progression towards the reconfiguration of STORM-3 into the desired humanoid formation

A similar Lagrangian derivation generates an equation of motion for the locomotion module in the form of

$$ \left\{\left(m_L\,{}^{L}d_C + \lambda m_M L\right)g - {}^{L}R\right\}\sin{}^{L}\theta(t) + \left({}^{L}T - {}^{L}f_{roll}\right)L\cos{}^{L}\theta(t) + {}^{L}\tau_J = \left(J_{LOK} + m_L\,{}^{L}d_C{}^2 + m_P L^2\cos^2\left({}^{L}\theta(t)\right)\right){}^{L}\ddot{\theta} \qquad (2) $$

where g defines gravity, and $\lambda < 1$ a scaling factor that reflects the share of the manipulation module's mass carried by the left locomotion module ($\lambda = 0.5$ for a symmetrical motion in Stage 3). ${}^{L}R$ can be calculated from the balance of dynamic forces, Note that in Stage 3, the central arm experiences a pure vertical translation, and therefore does not contribute to the rotational inertia of the formation.

B. Motion Scheduling and Synchronization Architecture

Using the equations of motion in (1) and (2), an optimal control problem can be formulated and solved to generate a control history for joints R_1 – R_4 and R_9, R_{10} during the scissor-like motion of Stage 3. In this formulation, we adopt the final time t_f as the cost functional, and re-write (1) and (2) into a system of non-linear state equations which we further combine with inequality constraints g_{ineq}, and boundary conditions h_0 (at $t = t_0$ corresponding to the beginning of Stage 3) and h_f (at $t = t_f$ corresponding to the end of Stage 3). The resulting problem can be written as

$$ \begin{aligned} &\textit{Min} \quad t_f \\ &\textit{subject to} \quad \dot{\chi} = f(\chi, t) \\ &\textit{and the constraints} \quad g_{ineq} = \begin{cases} \sup\left(\left|{}^{L}\tau_P\right|\right) < \tau_P^{\max} \\ \sup\left(\left|{}^{L}\tau_J\right|\right) < \tau_J^{\max} \end{cases} \qquad (3) \\ &\textit{with } h_0 = \begin{cases} {}^{L}\psi(0) = {}^{L}\psi_{init} \\ {}^{L}\theta(0) = {}^{L}\theta_{init} \\ {}^{L}\dot{\psi}(0) = {}^{L}\dot{\theta}(0) = 0 \end{cases} \quad \textit{and } h_f = \begin{cases} {}^{L}\psi(0) = {}^{L}\psi^{d} \\ {}^{L}\theta(0) = {}^{L}\theta^{d} \\ {}^{L}\dot{\psi}(0) = {}^{L}\dot{\theta}(0) = 0 \end{cases} \end{aligned} $$

where $\chi = \left[{}^{L}\psi \quad {}^{L}\dot{\psi} \quad {}^{L}\theta \quad {}^{L}\dot{\theta}\right]^T$ is the state vector, $f(\chi, t)$ the system of non-linear state equations extracted from (1) and (2), and $\tau_P^{\max}$, $\tau_J^{\max}$ the maximum joint torque for the pulleys and the docking joints, respectively (*sup* denotes the supremum). The optimality formulation in (3) can therefore be reiterated as the problem of finding the optimal control history ${}^{L}\psi$ or ${}^{L}\dot{\psi}$ and ${}^{L}\theta$ which can take a STORM-3 formation from the initial rest state h_0 (Stage 2-(d)), to the final desired state h_f – defined by ${}^{L}\psi^{d}$ and ${}^{L}\theta^{d}$ (Stage 3-(f)) – in minimum time without exceeding the joint torque thresholds.

The solution to (3) can be derived using an existing solver for two-point boundary value problems, such as the shooting method [21]. However, because the solution to a boundary value problem is neither unique nor guaranteed, it becomes prudent to also consider an alternative kinematic control scheme which correlates the motion of different joints by their trigonometric dependencies. That is, keeping the falling latter example in mind, one can relate the forward motion of the locomotion module to the vertical displacement of the arm to generate a kinematic control signal ${}^{L}\dot{\psi}(t, \theta(t))$ as

$$ {}^{L}\dot{\psi}(t, \theta(t)) = \begin{cases} 0 & t = t_0 \neq 0 \\ \dfrac{1}{t}\dfrac{\left\{L + r\cos{}^{L}\theta(t)\right\}}{r}\sin{}^{L}\theta(t) & t > t_0 \end{cases} \qquad (4) $$

which implicitly assumes a no-slip condition. In the event of slip, the forward displacement of the locomotion module will lag the rotation of joints R_9, R_{10}, which increases the latter torque as will be discussed subsequently. Such motion lead or lag can be captured by the optimal dynamic formulation in (3) rather than (4).

The control signal in (4) can then be integrated into an overall scheduling architecture implemented using sequential step functions with parabolic rise time, defined as

$$w(t) = \mathrm{K}\, step\left(t, t_{init}, 0, t_r, 1\right)$$

where K defines the value of w for $t > t_r$, and $step\left(t, t_{init}, 0, t_r, 1\right)$ parabolically interpolates $w(t)$ between the initial time t_{init} and the rise time t_r. An example of such scheduling is given in (5) and (6) for the actuation of R_9 and R_{10} from the beginning of Stage 1 up to the end of Stage 2

$$^{L}\theta(t) = -\left(\frac{\pi}{2}\right) step\left(t, 1.2, 0, 1.7, 1\right) \quad (5)$$

$$^{R}\theta(t) = \pi\, step\left(t, 0, 0, 1.1, 1\right) - \left(\frac{\pi}{2}\right) step\left(t, 1.2, 0, 1.7, 1\right) \quad (6)$$

These two functions are part of the chart plotted in Fig. 8(a).

IV. SIMULATIONS AND COMPARISON

Three simulation case-studies are reported in this section to highlight the motion scheduling control based on the kinematic scheme. These simulations also reflect the response of the robot to asynchronous control resulting in a motion lead or lag and their impact on joint torques, as captured in the dynamic formulation in (3).

In the kinematic case-study, the actuating functions for the active pulleys in Stage 3 are based on a selected constant angular velocity $\left|^{L}\dot{\psi}\right| = \left|^{R}\dot{\psi}\right| = 5 rad/s$ for $R_1 - R_4$. This generates a forward displacement of the locomotion modules that corresponds to a rotation of $^{L}\theta = +59°$ for R_9, and $^{R}\theta = -59°$ for R_{10} from Stage 2-(d) to 3-(f). The combined synchronous actuation signals are depicted in Fig. 8.

Using the CAE ACAR model of STORM-3 shown earlier in Fig. 5, a simulation of the kinematic synchronous case with the actuation signals of Fig. 8 was first accomplished to extract the torque histories on the actuated revolute joints. These are shown in red in Fig. 9(a) for R_9, R_{10}, and in Fig. 9(b)-(c) for $R_1 - R_4$. Albeit the kinematic control scheme is a deterministic approach which eliminates the likelihood of numerical divergence, it rather sacrifices the control flexibility of the robot and the ability to customarily share the torque load on the different joints involved in the reconfiguration process. Such flexibility is captured by the alternative control approach formulated in (3), where an adaptive control can be accomplished by tuning the dynamic parameters of the problem, such as manipulating the values of $\tau_P^{\max}$ and $\tau_J^{\max}$ for different payload scenarios.

Two examples of such adaptive control are illustrated in Fig. 9. For the first scenario, the extreme case where the pulleys are locked ($^{L}\dot{\psi} = {}^{R}\dot{\psi} = 0$) and the tracks are dragged on the ground is simulated. This corresponds to an unbounded $\sup(\left|^{L}\tau_J\right|)$, which generates a motion lag where the forward translation of the locomotion module is lagging the rotation of joints R_9 and R_{10}. Such behavior decreases the torque magnitude on $R_1 - R_4$ at the expense of an increased torque on R_9, R_{10}, as the latter become the sole contributor to the reconfiguration process at Stage 3 in this case.

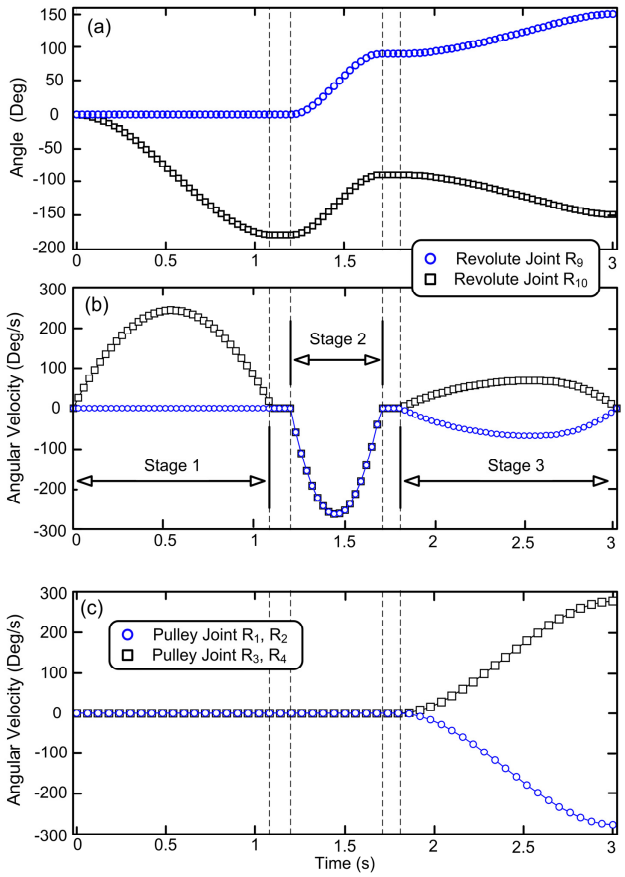

Fig. 8. Control functions for kinematic synchronous architecture from Stage 1 to Stage 3, (a) Angle history $^{L}\theta, {}^{R}\theta$ (b) Corresponding velocities $^{L}\dot{\theta}, {}^{R}\dot{\theta}$ and (c) Velocity signal $^{L}\dot{\psi}, {}^{R}\dot{\psi}$

Alternatively, the torque can be redistributed toward the pulleys to alleviate the load on joints R_9 and R_{10}. This is accomplished by creating a motion lead, where the locomotion modules are moving faster than R_9 and R_{10}, thereby reducing their torque while increasing the torque on the pulleys as shown in Fig. 9 (black plots). Such redistribution can be achieved by un-bounding $\sup(\left|^{L}\tau_P\right|)$, and capping $\sup(\left|^{L}\tau_J\right|)$ in (3) to a desired threshold. An ACAR simulation video of the reconfiguration process in this case-study can be found in [22].

Note that in Fig. 9, a simple moving average of order 8 was used to eliminate the spikes generated from integration errors. This filter distorts the torque plot during the transitional phase from Stage 2 to Stage 3. Also note that the high torque values in Fig. 9(a) are attributed to the large inertial dynamics generated in these simulations. This is because the reconfiguration process, from Stage 1 to 3, was

simulated in ~ 3 sec in order to minimize the convergence time of the CAE simulation. This time is amplified by the large number of degrees of freedom introduced by the track segments in these simulations. In reality, the execution time of this shape reconfiguration will be dictated by the dynamic torque load generated during this process, as well as by the torque capacity of the coupling interface [17].

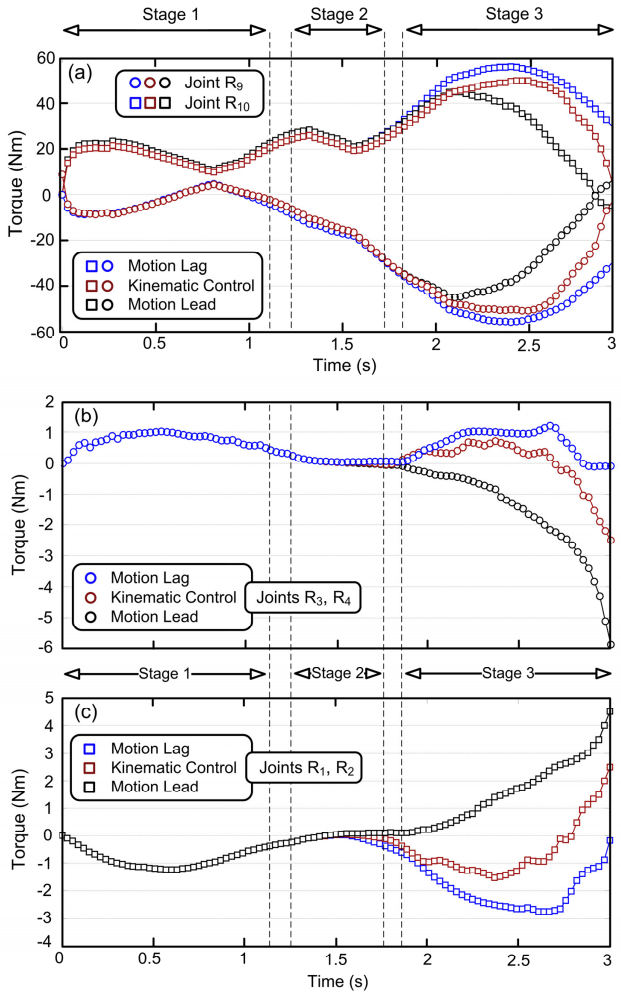

Fig. 9. Comparison of torque load on (a) Joints R_9, R_{10} (b) Joints R_3, R_4 (c) Joints R_1, R_2 , for both a kinematic control scheme (red), and for a dynamic control with a case of motion lag (blue) and motion lead (black) for the forward motion of the locomotion module.

V. CONCLUSION

This paper reported the study on motion scheduling and synchronization for a 3-module formation of STORM robot. The study is based on analytical and multi-body dynamic simulations which highlight the advantages and disadvantages of the proposed control methods (kinematic versus optimal dynamic). Such results will be further refined and tested in the future on a physical formation of STORM-3 as we continue the development of this robot.

ACKNOWLEDGMENT

The authors wish to thank the IT office at GWU for their hardware contributions to ADAMS CAR simulations.

REFERENCES

[1] P.M. Moubarak, and P. Ben-Tzvi, "Modular and Reconfigurable Mobile Robotics, *J. Robotics & Autonomous Systems*, vol. 60, no. 12, pp. 1648 – 1663, Dec. 2012.

[2] A. Kamimura, H. Kurokawa, E. Yoshida, S. Murata, K. Tomita, and S. Kokaji, "Automatic Locomotion Design and Experiments for a Modular Robotic System," *IEEE/ASME Transactions on Mechatronics*, vol. 10, no. 3, pp. 314 – 325, Jun. 2005.

[3] Z. Chen, and T. Iwasaki, "Circulant Synthesis of Central Pattern Generators with Application to Control of Rectifier Systems," *IEEE Transactions Automatic Control,* vol. 53, no. 1, pp. 273 – 286, Feb. 2008.

[4] J. Or, "A Hybrid CPG-ZMP Controller for the Real-Time Balance of a Simulated Flexible Spine Humanoid Robot," *IEEE Transactions on Systems, Man, & Cybernetics,* vol. 39, no. 5, pp. 547 – 561, Sept. 2009

[5] C. Liu, Q. Chen, and D. Wang, "CPG-Inspired Workspace Trajectory Generation and Adaptive Locomotion Control for Quadruped Robots," *IEEE Transactions on Systems, Man, and Cybernetics,* vol. 41, no. 3, pp. 867 – 880, Jun. 2011.

[6] G. Patel, M. Reid, D. Schimmel, and S. DeWeerth, "An Asynchronous Architecture for Modeling Intersegmental Neural Communication," *IEEE Transactions on Very Large Scale Integration (VLSI) Systems,* vol. 14, no. 2, pp. 97 – 110, Feb. 2006.

[7] R. Héliot, and B. Espiau, "Multisensor Input for CPG-Based Sensory-Motor Coordination," *IEEE Transactions on Robotics*, vol. 24, no. 1, pp. 191 – 195, Feb. 2008.

[8] C. Zhou, and K. H. Low, "Design and Locomotion Control of a Biomimetic Underwater Vehicle with Fin Propulsion," *IEEE/ASME Transactions on Mechatronics,* vol.1 7, no. 1, pp. 25 – 35, Feb. 2012.

[9] J. Kiener, and O. Von Stryk, "Towards Cooperation of Heterogeneous, Autonomous Robots: A Case Study of Humanoid and Wheeled Robots," *J. Robotics & Autonomous Systems,* vol. 58, no. 7, pp. 921 – 929, Jul. 2007.

[10] X. Zhu, Y. Kim, R. Merrell, and M. Minor, "Cooperative Motion Control and Sensing Architecture in Compliant Framed Modular Mobile Robots," *IEEE Trans. Robotics*, vol. 23, no. 5, pp. 1095 – 1101, Oct. 2007.

[11] A. Von Twickel, M. Hild, T. Siedel, V. Patel, and F. Pasemann, "Neural Control of a Modular Multi-Legged Walking Machine: Simulation and Hardware," *J. Robotics & Autonomous Systems,* vol. 60, no. 2, pp. 227 – 241, Feb. 2012.

[12] W. Zhao, Y. Hu, L. Zhang, and L. Wang, "Design and CPG-based Control of Biomimetic Robotic Fish," *IET Control Theory and Applications,* vol.3, no.3, pp. 281 – 293, Mar. 2009.

[13] P. Moubarak, and P. Ben-Tzvi, STORM Animation, 2011, http://www.seas.gwu.edu/~bentzvi/STORM/STORM_VR_Animation.html

[14] P. Ben-Tzvi, "Experimental Validation and Field Performance Metrics of a Hybrid Mobile Robot Mechanism", *Journal of Field Robotics*, vol. 27, no. 3, pp. 250 – 267, May 2010.

[15] P. Ben-Tzvi, A.A. Goldenberg, and J.W. Zu, "Design and Analysis of a Hybrid Mobile Robot Mechanism with Compounded Locomotion and Manipulation Capability", *Journal of Mechanical Design, Transactions of the ASME*, vol. 130, no. 7, pp. 1 – 13, July 2008.

[16] P. Ben-Tzvi, A.A. Goldenberg, and J.W. Zu, "Design, Simulations and Optimization of a Tracked Mobile Robot Manipulator with Hybrid Locomotion and Manipulation Capabilities", *Proceedings of the 2008 IEEE International Conference on Robotics and Automation (ICRA2008)*, Pasadena, California, 2008, pp. 2307 – 2312.

[17] P. Moubarak, P. Ben-Tzvi, "A Tri-State Rigid Reversible and Non-Back-Drivable Active Docking Mechanism for Modular Robotics," *IEEE/ASME Transactions on Mechatronics*, in press, 2013 (DOI: 10.1109/TMECH.2013.2261531).

[18] P. Moubarak, and P. Ben-Tzvi, "On the Dual-Rod Slider Rocker Mechanism and its Applications to Tristate Rigid Active Docking," *ASME Journal of Mechanisms and Robotics*, vol. 5, no. 1, p. 011010, Feb. 2013.

[19] P. Moubarak, E. Alvarez, P. Ben-Tzvi, Adams CAR Track Tension simulation: www.seas.gwu.edu/~bentzvi/STORM/TrackTensionSim.html, Available: Feb. 2013

[20] M. Freeman, and P. Muhoray, "On Mathematical and Physical Ladders," *American J. Physics*, vol. 53, no. 3, pp. 276 – 277, Mar. 1985.

[21] S. Roberts, and J. Shipman, "Two-Point Boundary Value Problems: Shooting Methods," *Elsevier Science Ltd.*, 1st Edition, 1972.

[22] P. Moubarak, E. Alvarez, and P. Ben-Tzvi, Adams CAR simulation of STORM-3 reconfiguration into a humanoid formation: www.seas.gwu.edu/~bentzvi/STORM/STORM3_Reconfiguration.html, Available: Feb. 2013.